



# HazMapper: A global open-source natural hazard mapping application in Google Earth Engine

Corey M. Scheip<sup>1,2</sup> and Karl W. Wegmann<sup>1,3</sup>

<sup>1</sup>Department of Marine, Earth, and Atmospheric Sciences, North Carolina State University, Raleigh, NC, 27695, USA

<sup>2</sup>North Carolina Geological Survey, Swannanoa NC, 28778, USA

<sup>3</sup>Center for Geospatial Analytics, North Carolina State University, Raleigh, NC, 27695, USA

**Correspondence:** Corey M. Scheip (cmscheip@ncsu.edu)

**Abstract.** Modern satellite networks with rapid repeat-cycles allow for near-real-time imaging of areas impacted by natural hazards such as mass wasting, flooding, and volcanic eruptions. Publicly accessible multi-spectral datasets (e.g. Landsat, Sentinel-2) are particularly helpful in analyzing the spatial extent of disturbances, however, the datasets are large and require intensive processing on high-powered computers by trained analysts. HazMapper is an open-access hazard mapping application developed in Google Earth Engine that allows users to derive map and GIS-based products from Sentinel or Landsat datasets without the time- and cost-intensive resources required for traditional analysis. Case studies are included for the identification of landslides and debris flows, wildfire burn extents, pyroclastic flows, and lava flow inundation. HazMapper is openly-available to the public and is intended for use by both scientists and non-scientists, such as emergency managers and public safety decision-makers. It is the intent of the authors to continue to develop HazMapper with additional capabilities. Collaboration on this effort is encouraged.

## 1 Introduction

Natural disasters such as landslides, wildfires, and volcanic eruptions are a primary mechanism of landscape change (Korup et al., 2010; Santi et al., 2013) while simultaneously causing fatalities in both developed and undeveloped nations into the 21<sup>st</sup> century (Froude and Petley, 2018; Petley, 2012; Auker et al., 2013; Holzer and Savage, 2013; Ashley and Ashley, 2008). As such, both Earth scientists and emergency managers have a keen interest in understanding natural disaster occurrences. Significant work is being performed on increasing predictive capabilities for natural hazard events (Goetz et al., 2015; Guzzetti et al., 2006) and a key component to these efforts is the robust characterization of modern-day events (Xu et al., 2016; Gallen et al., 2017).

Readily observable field evidence of only the largest or most recent natural disasters typically persist in vegetated landscapes and an unknown number of natural disasters have occurred prior to modern record keeping. Locating this field evidence and determining historical patterns of natural disasters is a primary objective for many agencies and communities (Wegmann, 2006;



Paton and Johnston, 2001; Brand et al., 2019). However, field work is often inefficient, expensive, provides a single time-stamp of ground conditions (e.g. the time of the field visit) and can only be performed by those with sufficient interest and resources.

25 The advent of rapid-repeat cycle satellite datasets (e.g. multi-spectral, thermal) has revolutionized the field of remotely sensing landscape changes on Earth. These data have been utilized since the 1970's (e.g. Landsat) to observe, monitor, and track landscape change (Lauer et al., 1997). In 2008, NASA began offering Landsat datasets for free to the general public via the internet (Woodcock et al., 2008) and by now, the entire archive is available online. Subsequent satellite networks (e.g. MODIS, Sentinel) have improved capabilities and increasingly complex satellite networks continue to be developed (e.g. Hoffman et al.,  
30 2016; Langhorst et al., 2019). Analysis of remote-sensing data has traditionally been performed by trained analysts on high-powered computers, often creating a resource-barrier for fiscally strained communities or those without advanced training.

Combining the open-access nature of these datasets with modern computational power available via cloud-computing is a recent development that has powerful implications for natural disaster monitoring (Kirschbaum et al., 2019). Google Earth Engine is a remote sensing data analysis platform designed to take advantage of Google's infrastructure for data storage, access,  
35 processing, and visualization (Gorelick et al., 2017). Aside from the obvious advantages of utilizing Google's computational resources, a key component of Google Earth Engine is the data catalog, removing the requirement for users to download and maintain large datasets, which are often gigabytes to petabytes in size. Google Earth Engine allows users to create public-facing applications, further increasing the accessibility of processing routines to specialists in the field as well as the scientific-curious public.

40 HazMapper (Hazard Mapper) is an open-access application developed in Google Earth Engine for the rapid characterization of natural disasters tailored to both the scientific and emergency management communities (Figure 1). HazMapper is useful for monitoring landscape change that results in the disruption of surface vegetation. While the underlying mathematics are not entirely novel, HazMapper democratizes multi-spectral satellite data processing with an emphasis on locating and characterizing natural hazards in vegetated regions. Select case studies are discussed here and include rainfall triggered mass wasting, seismically triggered mass wasting, wildfire burn extents, pyroclastic flows, and lava flow inundation following a volcanic fissure  
45 eruption. HazMapper is intended to foster community development surrounding rapid natural hazard mapping and characterization and we invite new ideas on leveraging the platform to easily, rapidly, and more precisely monitor Earth's dynamic surface and associated natural hazards. HazMapper is publicly accessible at <https://hazmapper.org/>.

## 2 Design Principles

50 Because HazMapper is intended to be a research and emergency management tool to evaluate current or historical disaster events, it is designed around user-input variables. Variables include dataset selection (e.g. Landsat 7, Landsat 8, Sentinel-2), event date, pre-event time window, post-event time window, and a slope threshold (Table 1). These variables can be updated throughout the use of the tool to aid in locating hazard-stricken areas. Base map options include Google's suite of global terrain and satellite basemaps. Resulting data layers are displayed in a layers pane, available for toggle, transparency adjustment, and  
55 download as spatially-referenced tagged image files (geoTIF).



Traditional remote sensing-based landslide mapping is performed by analysts observing change in aerial photographs (e.g. Malamud et al., 2004; Wegmann, 2006). This method relies on single pre- and post-event scenes and can be difficult given unfavorable atmospheric conditions. Optical aerial or satellite imagery is obscured by cloud cover, volcanic ash plumes, or other opaque atmospheric components. In the immediate aftermath of natural hazards that are initiated atmospherically (e.g. rainfall-triggered mass wasting) or volcanically (e.g. eruptions), it is not uncommon for imagery to be obscured by clouds or ash plumes, respectively. In cases of tropical or subtropical cyclones, cloud cover may persist for days to weeks following a disaster. Additionally, tropical regions of elevated rainfall and topography, and thus typical of mass wasting or flooding hazards, may experience cloud-cover for a substantial portion of the annual climate cycle.

To circumvent potentially opaque atmospheric conditions, HazMapper capitalizes on a technique within Google Earth Engine to generate and perform calculations on a greenest-pixel composite (Figure 2). The greenest pixel composite is a single composite image generated from all images within the user-defined pre- and post-event window that records the pixel with the highest normalized difference vegetation index (NDVI) result, or the “greenest” pixel (Eq. 1).

$$NDVI = \left( \frac{NIR - VIR}{NIR + VIR} \right) \quad (1)$$

Equation 1. NDVI calculation. NIR = Near-infrared, VIR = visible-infrared.

HazMapper relies on a relative difference in NDVI technique ( $rdNDVI$ , Eq. 2). Instead of differencing true color composites (i.e. red-green-blue bands), HazMapper exploits changes in surface vegetation by developing and differencing a NDVI-band from the greenest-pixel composite images. The results of the processing routine indicate a normalized percentage of NDVI gained or lost. The normalization parameter follows Ambrose et al. (2019), who propose this method for addressing pixel fractionation and the non-linear responsiveness of NDVI. Results may exceed +/- 100%. Loss of < -100% is possible due to the ability of VIR to increase to greater than the NIR value, causing a polarity change of NDVI. Results illustrate areas of the landscape that have either gained (increase in NDVI pixel-values) or lost (decrease in NDVI pixel-value) vegetation across the event as constrained by the pre-and-post event window date ranges. For visualization purposes, HazMapper applies a color-scale within the domain of -50% to +50%, simplifying the analysis to highlight areas with significant vegetative loss or gain. Additionally, an inspector tool allows a user to click anywhere within the map domain, upon which a latitude-longitude coordinate pair and the  $rdNDVI$  pixel value will be returned interactively to the user.

$$rdNDVI = \left( \frac{NDVI_{post} - NDVI_{pre}}{\sqrt{NDVI_{pre} + NDVI_{post}}} \right) \times 100 \quad (2)$$

Equation 2. Relative-difference in NDVI ( $rdNDVI$ ) equation.  $NDVI_{pre}$  = NDVI image of the pre-event greenest pixel composite.  $NDVI_{post}$  = NDVI image of the post-event greenest pixel composite.

The three resulting data layers (greenest pixel composite from pre- and post-event, and  $rdNDVI$ ) and a shuttle radar topography mission (SRTM) derived 30-m resolution hillshade layer (for areas between 60°N and 60°S latitude) are added to the standard Google Earth Engine layer pane. These layers can be toggled on/off and the transparency increased or decreased with



a slider to help with visualization. Available basemaps on the platform include Google's default suite of road, terrain, and satellite maps.

Heads-up digitization of areas of interest from the map domain, for example, debris flow initiation sites, landslide extents, or potential wildfire burn areas, can be recorded using Google's default mapping tools. Points, lines, and polygons may be digitized in one or multiple layers. During download from HazMapper, these digitized geometries can be saved as a keyhole-markup language (KML) file for viewing in Google Earth or sharing amongst an emergency response team or between research colleagues.

Additional sharing of HazMapper results is made available via the use of variable-tags within the URL. During usage of the tool, URL tags for the required event parameters are updated. Sharing of the updated link with a colleague or research partner allows that person to open HazMapper to the same viewport and updates the map function to the same event parameters. For this article and shared finds at HazMapper.org, we have utilized the North Carolina State University Go Links URL service. For example, <https://go.ncsu.edu/hazmapper-kenya> directs the user to the curated example of rainfall-triggered debris flows located in west Pokot County, Kenya, in November 2019 (see Section 4.1.1). All case studies discussed in this paper are available pre-loaded from the HazMapper launch screen, under the "Show Examples" tab, as well as at <https://hazmapper.org/>.

Data download is an important component of HazMapper. This function allows for enhanced use of the results, including incorporation into emergency operation mapping platforms and advanced scientific analysis. Downloads are distributed as single zip files containing single-band georeferenced TIF files. The user can download the 1) *rdNDVI* image, 2) pre-event and 3) post-event greenest-pixel composite images, 4) elevation and hillshade images derived from the global 30-m SRTM dataset and/or 5) any user-digitized geometries delineating points or areas of interest.

### 3 Earth Engine vs. Traditional GIS Environments

In the aftermath of large natural disasters, the level of emergency response can vary based on available resources for the region or country. For example, response efforts for a large landslide disaster in the United States, (e.g. 2014 Oso landslide, WA or 2019 Montecito, CA debris flows) can garner the attention and resources of local, state, and federal government agencies (Scholl and Carnes, 2017). In less affluent regions, however, response efforts may be significantly less intensive and timely, risking increased loss of life. An overarching goal of HazMapper is to bring modern, rapid scientific analysis and computing power to regions with less adequate resources.

Inventorying impacts following a natural disaster can be incredibly useful for researchers. Inventory efforts are time and resource-intensive (e.g., purchasing high-resolution aerial imagery or performing significant field verification efforts) and often experience time delays following the disaster (Malamud et al., 2004). HazMapper provides an opportunity for researchers to perform preliminary inventory work without field visits and without paying for commercial data products. Additionally, it allows researchers to time-stamp ground conditions. This is useful to understand the progression of disasters, such as continued wildfire spread or mass wasting initiated by earthquake aftershocks. Traditional GIS analysis requires significant digital storage capacity, computing power, and training. Even with modern personal computers, processing can take hours to days. Individual



120 scenes of Sentinel-2 datasets, for example, are typically hundreds of megabytes. Processing of these data also result in a  
fixed-extent output. Google Earth Engine's architecture initiates geospatial processing updates as the user navigates the map  
and, as such, HazMapper can be used to quickly evaluate spatially expansive hazards. HazMapper's source code initiates data  
processing on remote servers without requiring any specialized or licensed software and can be performed on any computer with  
an internet-browser and internet-connection. No software downloads are required and typical processing times on HazMapper  
125 are less than 1-2 minutes, allowing responders or researchers to adjust variables and visualization parameters to rapidly assess  
the potential impact of natural hazards at a specific location or across a region of interest.

#### 4 Case Studies

For many decades, researchers have utilized satellite-observed vegetation losses as a proxy for change on Earth's surface. The  
usefulness of satellite-observations in the scientific community are difficult to overstate and future developments (e.g. Hoffman  
130 et al., 2016) are increasing the need for enhanced processing methodologies and techniques. Some traditional uses for satellite-  
observations include identifying landslides and debris flows (e.g. Tillery and Rengers, 2019), wildfire (e.g. Miller and Thode,  
2007; Amos et al., 2019), volcanic monitoring (e.g. Cando-Jácome and Martínez-Graña, 2019), deforestation (e.g. Hansen  
et al., 2013; Green and Sussman, 1990; Ian), urban change and development (e.g. Masek et al., 2000; Schneider, 2012), and  
ecological monitoring and change detection (e.g. Zhou et al., 2001; Meentemeyer et al., 2004), amongst others.

135 HazMapper includes an example panel in the lower left of the tool, pointing the user to five real-world natural hazard case  
studies (Figure 1). The panel is intended to serve as a learning platform for new users to work with curated examples to explore  
these events. These five curated examples are discussed herein. The intent of these case studies is not to provide an exhaustive  
analysis of the events, but to showcase various applications of a *rdNDVI* cloud-computing method. HazMapper is intended  
to facilitate future research in the occurrence, characteristics, and impacts of global natural hazards.

#### 140 4.1 Mass Wasting

Landslide events are a primary contributor to topographic erosion and landscape evolution (Korup et al., 2010), make avail-  
able significant rock-bound and organic (soil and above ground biomass) carbon for global biogeochemical cycling (Hilton  
et al., 2008), and caused at least 55,997 non-seismic landslide fatalities between 2004-2016 and billions (\$) in global lost and  
damaged infrastructure costs (Froude and Petley, 2018; Emberson et al., 2020; Kirschbaum et al., 2015; Petley, 2012). In the  
145 United States alone, annual losses to mass wasting events exceed \$3 billion (Spiker and Gori, 2003; Burns, 2007).

Significant research has been performed on remotely detecting mass wasting events such as debris flows, debris slides, or  
rock slides. Pixel-based or object-oriented analysis (OOA) methods rely on characterizing change to the Earth surface via  
multi-spectral satellite imagery and correlating these changes to mass wasting events (e.g. Lu et al., 2019). Recognizing that in  
forested areas, landslides denude the landscape of vegetation, NDVI change detection methods have been used for identifying  
150 landslides in many mid-latitude regions (Huang et al., 2020; Tsai et al., 2010; Mondini et al., 2011; Lu et al., 2019; Yang  
et al., 2013). Until now, these methods were time consuming, considered one to a few pre- and post-event images, and required



analysis by trained professionals with access to high-powered computers and large digital storage capacity. Whether to provide emergency managers with a first look at impacts, or to assist in the first step of analysis for trained research professionals, HazMapper democratizes NDVI change detection methods for identifying mass wasting events.

#### 155 **4.1.1 Rainfall-triggered debris flows, West Pokot County, Kenya, 23 November 2019**

In mid-late November 2019, regions in eastern Africa experienced many days of intense rainfall, with some areas exceeding 5.5 meters of rainfall in a 7-day period (Huffman et al., 2014). West Pokot County, Kenya, located in the rugged terrain of the east African rift valley in western Kenya (Figure 3), received greater than 400mm of rainfall within the period 23-25 November (Huffman et al., 2014). This rainfall event triggered failures of steep, soil mantled hillslopes along the western rim  
160 of the east Africa Rift Valley (Elgeyo Escarpment), initiating fatal debris flows that destroyed homes, agricultural fields, and infrastructure. As early as December 4th, 2019 (11 days following the mass wasting event), suitable Sentinel-2 datasets were available and HazMapper was utilized to locate the debris flows (Figure 3; see Supplementary data). In addition to the location of debris flows, *rdNDVI* also captured assumed hyper-concentrated streamflow, where riparian vegetation was removed from the banks of lower-gradient rivers as they drain the mountainous terrain where the mass wasting occurred.

165 Debris flows in western Kenya are not unprecedented and the Elgeyo Escarpment, the steep terrain along the western edge of the Great Rift Valley, has experienced significant historical landsliding (Maina-Gichaba et al., 2013). The steep slopes result from normal faulting associated with extension of the Great Rift Valley and are overlain by up to 3 km of Miocene sediments and lava flows that in the tropical climate have weathered to produce thick, residual soils (Maina-Gichaba et al., 2013). Average rainfall for the area is >800mm annually (Maina-Gichaba et al., 2013), but is likely greater along steep valley  
170 walls due to orographic lifting (Hession and Moore, 2011). The resulting thick soils and ample moisture have led to significant agricultural development and the region is heavily dissected by a patchwork of agricultural fields. Occasionally, heavy rainfall couples with the thick sediment packages to produce shallow, primarily rainfall-triggered, mass wasting that initiates primarily high on valley walls.

The West Pokot County debris flow HazMapper example illustrates the pace at which rapid repeat-cycle optical imagery can  
175 be utilized to aid in the identification of hazard-stricken areas. Figure 3 demonstrates the results after a 0.5-month post-event window. The timing of suitable datasets for an initial look at disaster impacts will depend on the timing of a disaster relative to acquisition schedules of the Sentinel-2 or Landsat platforms and atmospheric conditions (e.g. cloud cover during or following a rainfall-triggered mass wasting event). Acquisition schedules are publicly available for both platforms and can be used in conjunction with HazMapper to help responders understand when suitable datasets may become available.

#### 180 **4.1.2 Seismically-triggered mass wasting, Southern Highlands, Papua New Guinea, $M_w$ 7.5, 25 February 2018**

On 25 February, 2018, a  $M_w$  7.5 earthquake struck in the Southern Highlands of Papua New Guinea (PNG) along the Papuan Fold and Thrust Belt (Wang et al., 2019), triggering thousands of mass wasting events, damming the Tagari River, and impacting numerous communities across the region. Over a span of 2 months, 5 aftershocks of  $M_w$  >6 struck the same region (Wang et al., 2019). Two years after the event, a mass wasting inventory is not available while communities are still impacted from



185 the sequence of earthquakes and hillslope failures. Fatalities from coseismic mass wasting events can increase significantly, up to an order of magnitude, greater than fatalities resulting from the earthquake itself (Budimir et al., 2014). The 2018 Papua New Guinea earthquake and associated mass wasting resulted in at least 160 fatalities (Wang et al., 2019), but the individual contributions (e.g. building collapse, burial by hillslope mass movements, etc) are not well understood for this event that occurred in a rural and remote part of the country.

190 Seismic shaking is a primary triggering mechanism for mass movement mobilization on steep mountain terrain. Coseismic mass wasting, therefore, strongly influences erosional budgets of mountain belts (Hovius et al., 1997; Keefer, 1994; Korup et al., 2010; Hilton et al., 2008). Keefer (2002) has demonstrated an empirical relationship based upon a global dataset between the moment magnitude of a mainshock and the maximum distance from the epicenter that seismically-induced landslides are likely to be observed for the entire earthquake sequence (including aftershocks). For this  $M_w$  7.5 earthquake, the corresponding  
195 predicted maximum distance is approximately 300 km. HazMapper was utilized to rapidly assess regions within several tens of kilometers from the epicenter and hundreds of slides and flows were located (Figure 4). Additional mass wasting was noted when expanding the analysis window to the predicted 300 km maximum distance based on the earthquake magnitude. Furthermore, we noted possible coseismic slides and flows as far as several hundred km west of the epicenter in the Maoke Mountains of Indonesia. Mass wasting is common in the region and these events could have unique triggers, however, restricting  
200 pre- and post-event time windows to as little as 2 months bracketing the  $M_w$  7.5 mainshock demonstrates consistent timing with the 25 February, 2018 earthquake. HazMapper provides both a past- and future-looking approach to develop robust spatial and temporal catalogs of coseismic mass wasting and the evaluation of empirical relationships between parameters such as moment magnitude, modified Mercalli intensity scale, depth, focal mechanism, regional lithology, topographic position, land use type, etc. as functions of the distance from an epicenter.

205 Due to difficulties in ascertaining high-temporal-resolution sequences of mass wasting events following seismic shaking, it is typically difficult to determine if particular events were triggered by just the mainshock or also by aftershocks. Thus, research to date has focused on earthquake sequences, inclusive of all associated shaking (e.g. Keefer, 2002). HazMapper allows researchers to temporally constrain landscape change and in certain circumstances, may be useful for understanding hillslope failure sequences when large aftershocks follow the main event. Future research should consider utilizing these time-  
210 stamped change detection images to understand the progression of failures during an earthquake sequence.

While identifying vegetative loss for locating geohazards is a key characteristic of a mass wasting event response, identifying subsequent vegetation recovery can serve as a proxy for the reduction of associated hazard (Shen et al., 2020). Simple modifications to event parameters in HazMapper, for example by changing the “event date” to a time after the occurrence of the disturbance event, can aid in observing vegetative recovery in landslide scars, suggesting establishment and growth of early  
215 successional species like grasses and shrubs (Figure 4-D). These stabilizing root masses buttress further soil loss and erosion, and, thus, decrease the associated downslope sediment transport from the zone of mass wasting.



## 4.2 Wildfire

Wildfire experts have been utilizing multi-temporal, multi-spectral imagery to evaluate burn extents following wildfires since at least the launch of the Landsat thematic mapper program in 1984 (Keeley, 2009; Miller and Thode, 2007; Cocke et al., 2005). Multi-spectral indices such as the popular Normalized Burn Ratio (NBR) and its derivatives (e.g. difference, relative difference) are widely employed to assess ecosystem impacts following a wildfire (Miller and Thode, 2007; Cocke et al., 2005). Discussion and debate about the most appropriate multi-spectral index to utilize for understanding fire impacts in wildland fire science are ongoing (Keeley, 2009; Miller and Thode, 2007; Escuin et al., 2008; Amos et al., 2019). The *rdNDVI* technique (Equation 2) utilized in HazMapper is one such index. It is our hope that future iterations of HazMapper will incorporate additional wildland fire specific burn indices allowing the user to select the index best suited for their specific research and operational purposes.

### 4.2.1 Chimney Tops 2 Fire, Tennessee, USA, November 2016

In the autumn of 2016, the southern Appalachian Mountains underwent intense drought conditions leading to dozens of wildfires that totaled some 75,000 acres (Andersen and Sugg, 2019). Originating within the Great Smoky Mountains National Park (GRSM), the Chimney Tops 2 fire was first discovered on 23 November, 2016 (National Park Service, 2017; Jiménez et al., 2018). The fire initially ignited on top of the north spire of Chimney Tops inside GRSM (Guthrie et al., 2017). Unexpected wind conditions facilitated the rapid expansion of the fire perimeter and fires were noted inside the city limits of Gatlinburg, TN, some 10 km from the ignition point, by 28 November (National Park Service, 2017; Guthrie et al., 2017). The Chimney Tops 2 fire burned 17,000 acres before eventually merging with other eastern Tennessee wildfires (Guthrie et al., 2017). Impacts from the fire included 14 fatalities, 14,000 evacuations, over 2,500 structures lost, an estimated \$2 billion in damages, and was the largest wildland fire in recorded history in the park (National Park Service, 2017; Guthrie et al., 2017).

HazMapper was utilized to observe vegetation loss, and by proxy, the severity and burn extent (Figure 5). In addition to the simple fire perimeter, the HazMapper method also illustrates burn severity by way of *rdNDVI*, highlighting that the most severe burn, as indicated by greater percent *rdNDVI* decreases, occurred along ridges and upper elevations, consistent with typical wildland fire behavior (Teie, 2018).

Following on the identification of vegetation loss, subsequent vegetative re-greening of the landscape after the fire is depicted as *rdNDVI* increases. Figures 5-B and 5-C illustrate recovery between the first through second growing seasons following the fire (2017 to 2018) and from the first through the third growing seasons (2017 to 2019), respectively. Future iterations of HazMapper could include more robust measures of re-greening. Forest recovery monitoring via remote sensing data is not a novel approach (Chen et al., 2014; Cuevas-González et al., 2009), however, the rapidity of observing the recovery via an open-access remote-processing and cloud-based platform is, to our knowledge, novel.



### 4.3 Volcanic Eruptions

Between 1600 to 2010 CE, 533 volcanic events have resulted in at least 278,880 fatalities (Auken et al., 2013). The number of fatalities each year attributable to volcanic events is increasing monotonically with time, suggesting that as a species, we are not overcoming the danger associated with volcanic hazards. As such, volcanologists have been using remote-sensing tools, particularly multi-spectral satellite data, as early as the mid-1980's to monitor volcanic heat signatures as precursors to eruptive activity (Rothery et al., 1988). The moderate resolution imaging spectrometer (MODIS) multi-spectral sensor is commonly used to monitor thermal characteristics and to detect volcanic eruptions (Wright et al., 2002), however, its variable 250 to 1000 meter pixel size inhibits the use of the platform for adequately identifying many downslope hazards associated with eruptions. Downslope hazards may include lava flows, ballistic projectiles, pyroclastic flows, and lahars (Blong, 1984). Following eruptions, HazMapper's use of 30-meter Landsat or 10-meter Sentinel-2 data is well suited to identify the spatial extent of these hazards, which may be only meters to tens of meters wide (e.g. a pyroclastic flow track) and may travel many kilometers from the volcano.

#### 4.3.1 Pyroclastic Flows, Volcan de Fuego, Antigua, Guatemala, 3 June 2018

Volcan de Fuego is a subduction zone stratovolcano located in southwestern Guatemala, near the city of Antigua. Since 1524, Fuego has produced 51 eruptions with a volcanic explosivity index  $\geq 2$  (Global Volcanism Program, 2013). The volcano is renowned for its consistent low-intensity Strombolian eruptions punctuated by larger, more violent sub-Plinian eruption cycles (Naismith et al., 2019). The most recent eruptive cycle of Fuego, ongoing since 2015, consists of an increase in paroxysmal eruptions and resulting downslope hazards (Naismith et al., 2019). The 3-5 June 2018 sub-Plinian eruption generated pyroclastic flows in excess of 11 km in length, resulted in hundreds of fatalities, and decimated the rural community of San Miguel Los Lotes (Pardini et al., 2019; Naismith et al., 2019).

HazMapper was utilized to observe landscape change following the 3-5 June 2018 Volcan de Fuego eruption (Figure 6). Summit effects of the eruption are observed via HazMapper, as well as pyroclastic flows down the west, south, and east flanks of the stratovolcano for up to 11km. Due to Fuego's consistent eruptive activity and loose, steep volcanic sediments, vegetation is generally sparse near the summit (Figure 6-B). However, as indicated by the *rdNDVI* results, loss of the limited-vegetation was evident on 30-meter Landsat data. In the analysis, one area directly east of the summit exhibited no vegetation loss (positive *rdNDVI* values), even though it is directly between the summit crater and a downslope pyroclastic flow, suggesting that this area is an example of an analytical false negative (Figure 6-D). Pyroclastic flows from the 3-5 June, 2018 eruption are evident in the main valleys draining away from the volcano and generally appear to transition to hyper-concentrated stream flows, some of which apparently resulted in channel-adjacent vegetation loss for >60 km to the south-southwest from the volcano, and in one case, reaching the Pacific Ocean (Figure 6-A).



#### 4.3.2 Lower East Rift Zone (LERZ) eruption, Kīlauea Volcano, Hawaii, USA, May-September 2018

Kīlauea is a basaltic shield volcano built from lavas derived from deep mantle driven processes. The magma feeding the volcano is distributed through a network of shallow rift structures and was pooled in a lava lake at its summit until commencement of the 2018 eruptive sequence. Eruptive characteristics have varied through time including a combination of periods of summit and/or rift eruptions, and caldera collapse, in-fill, and overflow (Holcomb, 1987). The most recent 2018 caldera collapse-rift eruption sequence was well captured by a dense array of scientific instrumentation and social networking, adding significant information to our present understanding of the Kīlauea complex (Neal et al., 2019). The 2018 event culminated in the inundation of 35.5 km<sup>2</sup> of Hawaii's Big Island and the destruction of hundreds of homes. Fortunately, there are no known fatalities from the event, likely due to the slow moving nature of the eruption and the significant resources applied during the disaster management response efforts.

HazMapper was utilized to observe surface changes within the Lower East Rift Zone (LERZ) following the cessation of the rift flank eruption sequence (Figure 7). Utilizing 30-meter Landsat data, the observed vegetation loss extending east and southeast from the LERZ approximates the published flow field from the 2018 eruption (Hawaiian Volcano Observatory staff, 2018). Efforts to utilize HazMapper to monitor the advancement of the lava flows were met with obscurity due to persistent cloud cover and volcanic gas emissions during the eruption. Additionally, the east-southeast extents of the lava flows generated additional landmass off of the coast of Hawaii, but with no vegetation to lose, this landscape change was not detected using HazMapper. Future code modifications may allow for the identification of the additional landmasses added to the island of Hawaii following the eruptions.

The 2018 Kīlauea eruption response benefited from significant resource application by way of the existing Hawaii Volcano Observatory and the associated resources of the U.S. federal and Hawaii state governments and associated scientific and resource protection agencies. This example, therefore, is highlighted to perform a first-order comparison of the kind of results available with HazMapper, a free and open-access toolset to an on-the-ground effort with significant financial, personnel, equipment, and computing resources and attention. For eruptions with less global attention or in more remote regions, remote sensing results like those available with HazMapper alone may approximate lava flow inundation extents, guiding future response efforts or scientific research around the event. Furthermore, the utilization of a consistent analysis platform between many eruptions may aid in volcanic research globally.

## 5 Conclusions

HazMapper is a free and open-access application developed in Google Earth Engine. It is primarily tailored to observing landscape change as a proxy for natural hazard impacts. The approach is novel, leveraging the power of Google Earth Engine to democratize change detection from multi-spectral satellite imagery in a user interface designed for researchers, emergency responders, and the scientific-curious public. HazMapper does not require users to download any datasets, possess a background in data analysis, software development, or coding, or have access to specialized software other than an internet-browser. And



because processing occurs remotely, low-powered computers (e.g. Google Chromebooks), tablet computers, and even mobile-  
310 enabled smart phones are suitable for use with HazMapper.

In version 1.0 of HazMapper, a single toolset is released for the observation of surface vegetation loss by way of a relative  
difference in NDVI values, suggesting the extents of hillslope and channelized mass wasting, wildfires, pyroclastic flows,  
and lava inundation hazards. Impacts from these hazards are located and described. In one example (Kenya mass wasting  
event), a rapid response is demonstrated by the location of features two weeks after they occurred. Research opportunities are  
315 demonstrated by creating a temporally constrained inventory of landslides associated with an earthquake (Papua New Guinea  
mass wasting event). Results from two heavily studied disasters - the Chimney Tops 2 wildfire and the Kīlauea volcanic eruption  
- demonstrate a good approximation of the published boundaries of extents of wildfire burn and lava flow fields, respectively.

There are several anticipated development opportunities for HazMapper. Principal amongst these is the development of  
hazard-specific platforms to provide more focused analysis for various hazard types. For example, a mass wasting platform  
320 could incorporate pixel segmentation, consideration of developed areas, and slope thresholds. Further research into the applica-  
tion of HazMapper in arid or snow-covered environments, including the consideration of snow-related indices (i.e. normalized  
difference snow index, NDSI), is on-going, and may be helpful for detecting mass wasting events in high-latitude or high-  
elevation regions. A wildfire platform can be expanded to include burn-specific indices such as NBR. And for all platforms, var-  
ious change detection methods (e.g. short-wave infrared differencing, amongst others) should continue to be evaluated. Radar  
325 data brings exciting opportunities, and as radar processing routines become available within GEE, they should be leveraged.

Future development of HazMapper will leverage new datasets as they become available. The initial release includes options  
to analyze Sentinel-2, Landsat 8, and Landsat 7 datasets. HazMapper's underlying codeset is designed to be easy to add  
forthcoming datasets, such as Landsat 9 that is anticipated to launch in December 2020 (McCorkel et al., 2018).

At the time of this publication, the features discussed herein have been tested, however, it should be noted that GEE is  
330 a rapidly evolving technology. As changes are made within GEE, we will maintain HazMapper to the best of our ability,  
including maintaining existing functionality and adding functionality as technology permits. HazMapper is an open-source  
project and community contributions are welcomed. Supporting JavaScript codesets for HazMapper are available at <https://hazmapper.org/code>.

*Code and data availability.* Code will be available at time of publication for collaboration and will be accessible at <https://hazmapper.org/>  
335 code. Once gaining permissions to HazMapper (see letter to the editors), case studies discussed in this article can be accessed from the  
following URLs. Once accepted for publication, these URLs will work for the general public.

- Rainfall-triggered mass wasting, West Pokot County, Kenya, 23 November 2019: <https://go.ncsu.edu/hazmapper-kenya>
- Seismically-triggered mass wasting, Southern Highlands, Papua New Guinea, M 7.5, 25 February 2018: <https://go.ncsu.edu/hazmapper-png>
- Chimney Tops 2 Wildfire, Tennessee, USA, November 2016: <https://go.ncsu.edu/hazmapper-chimneytops>
- 340 – Pyroclastic flows, Volcan de Fuego, Antigua, Guatemala, 3 June 2018: <https://go.ncsu.edu/hazmapper-fuego>
- Lower East Rift Zone eruption, Kilauea Volcano, Hawaii, USA, May-September 2018: <https://go.ncsu.edu/hazmapper-lerz>



*Author contributions.* CMS and KWW made significant contributions to the design and execution of building HazMapper, including the source code, website, and this article. Both authors gave final approval of this manuscript.

*Competing interests.* The authors declare that no competing interests are present.

345 *Acknowledgements.* We gratefully acknowledge Steve P. Norman of the U.S. Forest Service Southern Research Station in Asheville, NC for helpful early conversations regarding the mathematics behind the *rdNDVI* techniques he has been using for wildland fire studies. Additional thanks are owed to Dr. Jesse Hill of the North Carolina Geological Survey for helpful discussions regarding the use of the *rdNDVI* technique in observing debris flows in western North Carolina and for his input on the HazMapper user interface.



## References

350

Ambrose, M. J., Berryman, E. M., Canavin, J. C., Christie, W. M., Coulston, J. W., Eager, T., Koch, F. H., Norman, S. P., O'Dea, C. B., Paschke, J. L., and Potter, K. M.: Analyses of Long-Term Forest Health Trends and Presentations of New Techniques, Chapter 7. Satellite-based Evidence of Forest Stress and Decline across the Conterminous United States for 2016, 2017, and 2018, in: DRAFT Forest Health Monitoring: National Status Trends, and Analysis 2019, edited by Potter, K. M. and Conkling, B. L., pp. 135–150, 2019.

355 Amos, C., Petropoulos, G. P., and Ferentinos, K. P.: Determining the use of Sentinel-2A MSI for wildfire burning & severity detection, *International Journal of Remote Sensing*, 40, 905–930, <https://doi.org/10.1080/01431161.2018.1519284>, <https://doi.org/10.1080/01431161.2018.1519284>, 2019.

Andersen, L. M. and Sugg, M. M.: Geographic multi-criteria evaluation and validation: A case study of wildfire vulnerability in Western North Carolina, USA following the 2016 wildfires, *International Journal of Disaster Risk Reduction*, 39, 101–123, <https://doi.org/10.1016/j.ijdr.2019.101123>, <https://doi.org/10.1016/j.ijdr.2019.101123>, 2019.

360 Ashley, S. T. and Ashley, W. S.: Flood fatalities in the United States, *Journal of Applied Meteorology and Climatology*, 47, 805–818, <https://doi.org/10.1175/2007JAMC1611.1>, 2008.

Auker, M. R., Stephen, R., Sparks, J., Siebert, L., Croweller, H. S., and Ewert, J.: A statistical analysis of the global historical volcanic fatalities record, *Journal of Applied Volcanology*, 2, 1–24, <https://doi.org/10.1186/2191-5040-2-2>, 2013.

365 Blong, R.: *Volcanic Hazards*, 424 pp, Academic Press, Sydney, 1984.

Brand, B. D., Schlegel, M., and McMullin-Messier, P.: “Map Your Hazards!”: Assessing Hazards, Vulnerability, and Risk Through an Active Learning-Based Educational Module, in: *Interdisciplinary Teaching About Earth and the Environment for a Sustainable Future*, pp. 213–231, Springer, 2019.

Budimir, M. E., Atkinson, P. M., and Lewis, H. G.: Earthquake-and-landslide events are associated with more fatalities than earthquakes alone, *Natural Hazards*, 72, 895–914, <https://doi.org/10.1007/s11069-014-1044-4>, 2014.

370 Burns, S.: February 2007 - Prevention Is the Best Medicine, [http://www.geotimes.org/feb07/feature\\_prevention.html](http://www.geotimes.org/feb07/feature_prevention.html), 2007.

Cando-Jácome, M. and Martínez-Graña, A.: Determination of primary and secondary lahar flow paths of the Fuego Volcano (Guatemala) using morphometric parameters, *Remote Sensing*, 11, <https://doi.org/10.3390/rs11060727>, 2019.

Chen, W., Moriya, K., Sakai, T., Koyama, L., and Cao, C.: Monitoring of post-fire forest recovery under different restoration modes based on time series Landsat data, *European Journal of Remote Sensing*, 47, 153–168, <https://doi.org/10.5721/EuJRS20144710>, 2014.

Cocke, A. E., Fulé, P. Z., and Crouse, J. E.: Comparison of burn severity assessments using Differenced Normalized Burn Ratio and ground data, *International Journal of Wildland Fire*, 14, 189–198, <https://doi.org/10.1071/WF04010>, 2005.

Cuevas-González, M., Gerard, F., Balzter, H., and Riaño, D.: Analysing forest recovery after wildfire disturbance in boreal Siberia using remotely sensed vegetation indices, *Global Change Biology*, 15, 561–577, <https://doi.org/10.1111/j.1365-2486.2008.01784.x>, 2009.

380 Emberson, R., Kirschbaum, D., and Stanley, T.: New Global Characterization of Landslide Exposure, *Nat. Hazards Earth Syst. Sci. Discuss.*, 2020, 1–21, <https://doi.org/10.5194/nhess-2019-434>, <https://www.nat-hazards-earth-syst-sci-discuss.net/nhess-2019-434/> <https://www.nat-hazards-earth-syst-sci-discuss.net/nhess-2019-434/nhess-2019-434.pdf>, 2020.

Escuin, S., Navarro, R., and Fernández, P.: Fire severity assessment by using NBR (Normalized Burn Ratio) and NDVI (Normalized Difference Vegetation Index) derived from LANDSAT TM/ETM images, *International Journal of Remote Sensing*, 29, 1053–1073, <https://doi.org/10.1080/01431160701281072>, 2008.

385



- Froude, M. J. and Petley, D. N.: Global fatal landslides 2004 to 2016, *Natural Hazards and Earth System Sciences*, 18, 2161–2181, <https://www.arcgis.com/apps/webappviewer/index.html?id=98462998953c4f1fbd7caaa166373f63>, 2018.
- Gallen, S. F., Clark, M. K., Godt, J. W., Roback, K., and Niemi, N. A.: Application and evaluation of a rapid response earthquake-triggered landslide model to the 25 April 2015 Mw 7.8 Gorkha earthquake, Nepal, *Tectonophysics*, 714–715, 173–187, <https://doi.org/10.1016/j.tecto.2016.10.031>, <http://dx.doi.org/10.1016/j.tecto.2016.10.031>, 2017.
- Global Volcanism Program: Fuego (342090) in *Volcanoes of the World*, v. 4.8.6. Venzke, E (ed.). Smithsonian Institution. Downloaded 26 Feb 2020 (<https://volcano.si.edu/volcano.cfm?vn=342090>), <https://doi.org/https://doi.org/10.5479/si.GVP.VOTW4-2013>, 2013.
- Goetz, J. N., Brenning, A., Petschko, H., and Leopold, P.: Evaluating machine learning and statistical prediction techniques for landslide susceptibility modeling, *Computers and Geosciences*, 81, 1–11, <https://doi.org/10.1016/j.cageo.2015.04.007>, <http://dx.doi.org/10.1016/j.cageo.2015.04.007>, 2015.
- Gorelick, N., Hancher, M., Dixon, M., Ilyushchenko, S., Thau, D., and Moore, R.: Google Earth Engine: Planetary-scale geospatial analysis for everyone, *Remote Sensing of Environment*, 202, 18–27, <https://doi.org/10.1016/j.rse.2017.06.031>, <https://doi.org/10.1016/j.rse.2017.06.031>, 2017.
- Green, G. M. and Sussman, R. W.: Deforestation history of the eastern rain forests of Madagascar from satellite images, <https://doi.org/10.1126/science.248.4952.212>, 1990.
- Guthrie, V., Finucane, M., Keith, P., and Stinnett, D.: After Action Review of the November 28, 2016, Firestorm, p. 164, [http://wildfiretoday.com/documents/AAR\[\\_\]ChimneyTops2.pdf](http://wildfiretoday.com/documents/AAR[_]ChimneyTops2.pdf), 2017.
- Guzzetti, F., Reichenbach, P., Ardizzone, F., Cardinali, M., and Galli, M.: Estimating the quality of landslide susceptibility models, *Geomorphology*, 81, 166–184, <https://doi.org/10.1016/j.geomorph.2006.04.007>, 2006.
- Hansen, M., Potapov, P., Moore, R., Hancher, M., Turubanova, S., Tyukavina, A., Thau, D., Stehman, S., Goetz, S., Loveland, T., Komareddy, A., Egorov, A., Chini, L., Justice, C., and Townshend, J.: High-Resolution Global Maps of 21st-Century Forest Cover Change, *Science*, 342, 850–853, <https://doi.org/10.1126/science.1244693>, 2013.
- Hawaiian Volcano Observatory staff: Preliminary map of the 2018 lower East Rift Zone eruption of Kilauea Volcano, Island of Hawai‘i: U.S. Geological Survey, <https://doi.org/https://doi.org/10.5066/P994OGY8>, 2018.
- Hession, S. L. and Moore, N.: A spatial regression analysis of the influence of topography on monthly rainfall in East Africa, *International Journal of Climatology*, 31, 1440–1456, <https://doi.org/10.1002/joc.2174>, 2011.
- Hilton, R. G., Galy, A., and Hovius, N.: Riverine particulate organic carbon from an active mountain belt: Importance of landslides, *Global Biogeochemical Cycles*, 22, 1–12, <https://doi.org/10.1029/2006GB002905>, 2008.
- Hoffman, J. P., Shaffer, S., and Perkovic-Martin, D.: NASA L-SAR instrument for the NISAR (NASA-ISRO) Synthetic Aperture Radar mission, *Earth Observing Missions and Sensors: Development, Implementation, and Characterization IV*, 9881, 988 108, <https://doi.org/10.1117/12.2228489>, 2016.
- Holcomb, R. T.: Eruptive history and long-term behavior of Kilauea Volcano (Hawaii), 1987.
- Holzer, T. L. and Savage, J. C.: Global earthquake fatalities and population, *Earthquake Spectra*, 29, 155–175, <https://doi.org/10.1193/1.4000106>, 2013.
- Hovius, N., Stark, C. P., and Allen, P. A.: Sediment flux from a mountain belt derived by landslide mapping, *Geology*, 25, 231–234, [https://doi.org/10.1130/0091-7613\(1997\)025<0231:SFFAMB>2.3.CO;2](https://doi.org/10.1130/0091-7613(1997)025<0231:SFFAMB>2.3.CO;2), 1997.
- Huang, Q., Wang, C., Meng, Y., Chen, J., and Yue, A.: Landslide Monitoring Using Change Detection in Multitemporal Optical Imagery, *IEEE Geoscience and Remote Sensing Letters*, 17, 312–316, <https://doi.org/10.1109/LGRS.2019.2918254>, 2020.



- Huffman, G., Bolvin, D., Braithwaite, D., Hsu, K., Joyce, R., and Xie, P.: Integrated Multi-satellite Retrievals for GPM (IMERG), NASA's  
425 Precipitation Processing Center, Version 4.4, accessed: 2020-01-24, 2014.
- Jiménez, P. A., Muñoz-Esparza, D., and Kosović, B.: A high resolution coupled fire-atmosphere forecasting system to minimize the impacts  
of wildland fires: Applications to the Chimney Tops II wildland event, *Atmosphere*, 9, <https://doi.org/10.3390/atmos9050197>, 2018.
- Keefer, D. K.: The importance of earthquake-induced landslides to long-term slope erosion and slope-failure hazards in seismically active  
regions, *Geomorphology*, 10, 265–284, <https://doi.org/10.1016/b978-0-444-82012-9.50022-0>, 1994.
- 430 Keefer, D. K.: Investigating landslides caused by earthquakes - A historical review, *Surveys in Geophysics*, 23, 473–510,  
<https://doi.org/10.1023/A:1021274710840>, 2002.
- Keeley, J. E.: Fire intensity, fire severity and burn severity: A brief review and suggested usage, *International Journal of Wildland Fire*, 18,  
116–126, <https://doi.org/10.1071/WF07049>, 2009.
- Kirschbaum, D., Stanley, T., and Zhou, Y.: Spatial and temporal analysis of a global landslide catalog, *Geomorphology*, 249, 4–15,  
435 <https://doi.org/10.1016/j.geomorph.2015.03.016>, <http://dx.doi.org/10.1016/j.geomorph.2015.03.016>, 2015.
- Kirschbaum, D., Watson, C. S., Rounce, D. R., Shugar, D. H., Kargel, J. S., Haritashya, U. K., Amatya, P., Shean, D., Anderson, E. R.,  
and Jo, M.: The State of Remote Sensing Capabilities of Cascading Hazards Over High Mountain Asia, *Frontiers in Earth Science*, 7,  
<https://doi.org/10.3389/feart.2019.00197>, 2019.
- Korup, O., Densmore, A. L., and Schlunegger, F.: The role of landslides in mountain range evolution, *Geomorphology*, 120, 77–90,  
440 <https://doi.org/10.1016/j.geomorph.2009.09.017>, <http://dx.doi.org/10.1016/j.geomorph.2009.09.017>, 2010.
- Langhorst, T., Pavelsky, T. M., Frasson, R. P. d. M., Wei, R., Domeneghetti, A., Altenau, E. H., Durand, M. T., Minear, J. T., Wegmann,  
K. W., and Fuller, M. R.: Anticipated improvements to river surface elevation profiles from the surface water and ocean topography  
mission, *Frontiers in Earth Science*, 7, 1–13, <https://doi.org/10.3389/feart.2019.00102>, 2019.
- Lauer, D. T., Morain, S. A., and Salomonson, V. V.: The landsat program: Its origins, evolution, and impacts, *Photogrammetric Engineering  
445 and Remote Sensing*, 63, 831–838, 1997.
- Lu, P., Qin, Y., Li, Z., Mondini, A. C., and Casagli, N.: Landslide mapping from multi-sensor data through improved change detection-based  
Markov random field, *Remote Sensing of Environment*, <https://doi.org/10.1016/j.rse.2019.111235>, 2019.
- Maina-Gichaba, C., Kipseba, E. K., and Masibo, M.: Overview of Landslide Occurrences in Kenya. Causes, Mitigation, and Challenges,  
vol. 16, Elsevier B.V., 1 edn., <https://doi.org/10.1016/B978-0-444-59559-1.00020-7>, <http://dx.doi.org/10.1016/B978-0-444-59559-1.00020-7>, 2013.
- 450 Malamud, B. D., Turcotte, D. L., Guzzetti, F., and Reichenbach, P.: Landslide inventories and their statistical properties, *Earth Surface  
Processes and Landforms*, 29, 687–711, <https://doi.org/10.1002/esp.1064>, 2004.
- Masek, J. G., Lindsay, F. E., and Goward, S. N.: Dynamics of urban growth in the Washington DC metropolitan area, 1973-1996, from  
Landsat observations, *International Journal of Remote Sensing*, 21, 3473–3486, <https://doi.org/10.1080/014311600750037507>, 2000.
- 455 McCorkel, J., Montanaro, M., Efremova, B., Pearlman, A., Wenny, B., Lunsford, A., Simon, A., Hair, J., Reuter, D., Goddard, N., and Flight,  
S.: LANDSAT 9 Thermal Infrared Sensor 2 Characterization Plan Overview, IGARSS 2018 - 2018 IEEE International Geoscience and  
Remote Sensing Symposium, pp. 8845–8848, <https://doi.org/10.1109/IGARSS.2018.8518798>, 2018.
- Meentemeyer, R., Rizzo, D., Mark, W., and Lotz, E.: Mapping the risk of establishment and spread of sudden oak death in California, *Forest  
Ecology and Management*, 200, 195–214, <https://doi.org/10.1016/j.foreco.2004.06.021>, 2004.
- 460 Miller, J. D. and Thode, A. E.: Quantifying burn severity in a heterogeneous landscape with a relative version of the delta Normalized Burn  
Ratio (dNBR), *Remote Sensing of Environment*, 109, 66–80, <https://doi.org/10.1016/j.rse.2006.12.006>, 2007.



- Mondini, A. C., Guzzetti, F., Reichenbach, P., Rossi, M., Cardinali, M., and Ardizzone, F.: Semi-automatic recognition and mapping of rainfall induced shallow landslides using optical satellite images, *Remote Sensing of Environment*, 115, 1743–1757, <https://doi.org/10.1016/j.rse.2011.03.006>, 2011.
- 465 Naismith, A. K., Matthew Watson, I., Escobar-Wolf, R., Chigna, G., Thomas, H., Coppola, D., and Chun, C.: Eruption frequency patterns through time for the current (1999–2018) activity cycle at Volcán de Fuego derived from remote sensing data: Evidence for an accelerating cycle of explosive paroxysms and potential implications of eruptive activity, *Journal of Volcanology and Geothermal Research*, 371, 206–219, <https://doi.org/10.1016/j.jvolgeores.2019.01.001>, <https://doi.org/10.1016/j.jvolgeores.2019.01.001>, 2019.
- National Park Service: Chimney Tops 2 Fire Review Individual Fire Review Report, p. 116, <https://www.wildfirelessons.net/orphans/viewincident?DocumentKey=5bfa19b8-ca1e-4f4a-882f-9dad173ec28c>, 2017.
- 470 Neal, C., Brantley, S., Antolik, L., Babb, J., Burgess, M., Calles, K., Cappos, M., Chang, J., Conway, S., Desmithier, L., Dotray, P., Elias, T., Fukunaga, P., Fuke, S., Johanson, I., Kamibayashi, K., Kauahikaua, J., Lee, R., Pekalib, S., Miklius, A., Million, W., Moniz, C., Nadeau, P., Okubo, P., Parcheta, C., Patrick, M., Shiro, B., Swanson, D., Tollet, W., Trusdell, F., Younger, E., Zoeller, M., Montgomery-Brown, E., Anderson, K., Poland, M., Ball, J., Bard, J., Coomb, M., Dieterich, H., Kern, C., Thelen, W., Cervelli, P., Orr, T., Houghton, B., Gansecki, C., Hazlett, R., Lundgren, P., Diefenbach, A., Lerner, A., Waite, G., Kelly, P., Clor, L., Werner, C., Mulliken, K., Fisher, G., and Damby, D.: The 2018 rift eruption and summit collapse of Kīlauea Volcano, *Science*, 363, 367–374, 2019.
- Pardini, F., Queißer, M., Naismith, A., Watson, I. M., Clarisse, L., and Burton, M. R.: Initial constraints on triggering mechanisms of the eruption of Fuego volcano (Guatemala) from 3 June 2018 using IASI satellite data, *Journal of Volcanology and Geothermal Research*, 376, 54–61, <https://doi.org/10.1016/j.jvolgeores.2019.03.014>, 2019.
- 480 Paton, D. and Johnston, D.: Disasters and communities: vulnerability, resilience and preparedness, *Disaster Prevention and Management: An International Journal*, 2001.
- Petley, D.: Global patterns of loss of life from landslides, *Geology*, 40, 927–930, <https://doi.org/10.1130/G33217.1>, 2012.
- Rothery, D. A., Francis, P. W., and Wood, C. A.: Volcano monitoring using short wavelength infrared data from satellites, *Journal of Geophysical Research*, 93, 7993–8008, <https://doi.org/10.1029/JB093iB07p07993>, 1988.
- 485 Santi, P., Cannon, S., and DeGraff, J.: *Wildfire and landscape change*, chap. 13.16, Elsevier, 2013.
- Schneider, A.: Monitoring land cover change in urban and peri-urban areas using dense time stacks of Landsat satellite data and a data mining approach, *Remote Sensing of Environment*, 124, 689–704, <https://doi.org/10.1016/j.rse.2012.06.006>, <http://dx.doi.org/10.1016/j.rse.2012.06.006>, 2012.
- Scholl, H. J. and Carnes, S. L.: Managerial challenges in early disaster response: The case of the 2014 Oso/SR530 landslide disaster, *Proceedings of the International ISCRAM Conference, 2017-May*, 961–972, 2017.
- 490 Shen, P., Zhang, L. M., Fan, R. L., Zhu, H., and Zhang, S.: Declining geohazard activity with vegetation recovery during first ten years after the 2008 Wenchuan earthquake, *Geomorphology*, 352, 106 989, <https://doi.org/10.1016/j.geomorph.2019.106989>, <https://doi.org/10.1016/j.geomorph.2019.106989>, 2020.
- Spiker, E. C. and Gori, P.: National landslide hazards mitigation strategy, a framework for loss reduction, 1244, US Geological Survey, 2003.
- 495 Teie, W. C.: *Firefighter’s Handbook on Wildland Firefighting: Strategy, Tactics, and Safety*, Fire Protection Publications, 4 edn., Stillwater, OK, 2018.
- Tillery, A. C. and Rengers, F. K.: Controls on debris-flow initiation on burned and unburned hillslopes during an exceptional rainstorm in southern New Mexico, USA, *Earth Surface Processes and Landforms*, <https://doi.org/10.1002/esp.4761>, 2019.



- 500 Tsai, F., Hwang, J. H., Chen, L. C., and Lin, T. H.: Post-disaster assessment of landslides in southern Taiwan after 2009 Typhoon Morakot  
using remote sensing and spatial analysis, *Natural Hazards and Earth System Science*, 10, 2179–2190, <https://doi.org/10.5194/nhess-10-2179-2010>, 2010.
- USGS: US Geological Survey Geospatial Multi-Agency Coordination (GeoMAC) Wildland Fire Perimeters, data retrieved 21 February, 2020  
from USGS GeoMAC database, <https://rmgsc.cr.usgs.gov/outgoing/GeoMAC/>, 2020.
- Wang, S., Xu, C., Li, Z., Wen, Y., and Song, C.: 7.5 Papua New Guinea earthquake: A possible complex multiple faults failure event with  
505 deep-seated reverse faulting Shuai Wang, *Earth and Space Science*, pp. 0–2, <https://doi.org/10.1029/2019EA000966>, 2019.
- Wegmann, K.: Digital Landslide Inventory for the Cowlitz County Urban Corridor, Washington, Report of Investigations 35, [ftp://152.1.40.200/array1/ftp/reprints/Wegmann\\_{\\_}2006\\_{\\_}text.pdf](ftp://152.1.40.200/array1/ftp/reprints/Wegmann_{_}2006_{_}text.pdf), 2006.
- Woodcock, C. E., Allen, R., Anderson, M., Belward, A., Bindschadler, R., Cohen, W., Gao, F., Goward, S. N., Helder, D., Helmer, E.,  
Nemani, R., Oreopoulos, L., Schott, J., Thenkabail, P. S., Vermote, E. F., Vogelmann, J., Wulder, M. A., and Wynne, R.: Free Access to  
510 Landsat Imagery, *Science*, 320, 1011a–1011a, <https://doi.org/10.1126/science.320.5879.1011a>, 2008.
- Wright, R., Flynn, L., Garbeil, H., Harris, A., and Pilger, E.: Automated volcanic eruption detection using MODIS, *Remote Sensing of  
Environment*, 82, 135–155, [https://doi.org/10.1016/S0034-4257\(02\)00030-5](https://doi.org/10.1016/S0034-4257(02)00030-5), 2002.
- Xu, C., Xu, X., Tian, Y., Shen, L., Yao, Q., Huang, X., Ma, J., Chen, X., and Ma, S.: Two comparable earthquakes produced greatly  
different coseismic landslides: The 2015 Gorkha, Nepal and 2008 Wenchuan, China events, *Journal of Earth Science*, 27, 1008–1015,  
515 <https://doi.org/10.1007/s12583-016-0684-6>, 2016.
- Yang, W., Wang, M., and Shi, P.: Using MODIS NDVI time series to identify geographic patterns of landslides in vegetated regions, *IEEE  
Geoscience and Remote Sensing Letters*, 10, 707–710, <https://doi.org/10.1109/LGRS.2012.2219576>, 2013.
- Zhou, L., Tucker, C. J., Kaufmann, R. K., Slayback, D., Shabanov, N. V., and Myneni, R. B.: Variations in northern vegetation activity  
inferred from satellite data of vegetation index during 1981 to 1999, *Journal of Geophysical Research Atmospheres*, 106, 20 069–20 083,  
520 <https://doi.org/10.1029/2000JD000115>, 2001.



**Table 1.** HazMapper input variables, definitions, and examples.

Input Variables	Definition	Example
Dataset	Dataset to use for analysis. Currently Landsat 7, Landsat 8, or Sentinel-2	Sentinel-2 (10m) 2015+
Event Date	Date of storm, earthquake, weather event, etc.	9 December 2016
Pre-Event Window	The number of months to use for observing the greenest pixel-by-pixel conditions prior to the event	12
Post-Event Window	The number of months to use for observing the greenest pixel-by-pixel conditions following the event	3
Maximum Cloud Cover	The maximum percentage of a scene obscured by clouds and still used in the analysis. The cloud-cover percent is embedded in the metadata for each Landsat or Sentinel scene.	30
Slope Threshold	A minimum topographic slope value in degrees, less than which will be omitted from the data visualization. This is helpful to remove water bodies like lakes and adjacent oceans in coastal regions.	0.01

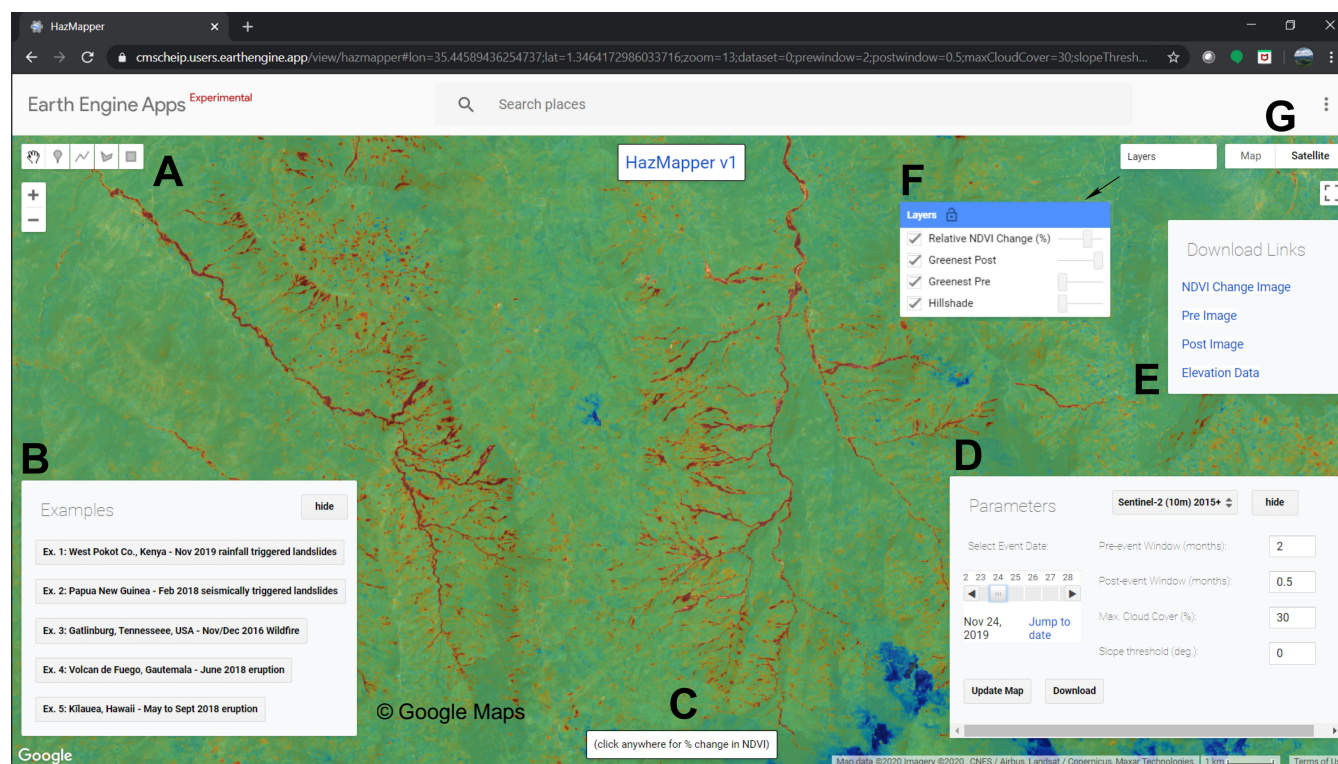


**Figure 1.** User interface of the HazMapper application in Google Earth Engine. Moving counterclockwise around the interface: A) Digitization tools allow the user to heads up digitize features of interest as points, lines, or polygons. B) An example window allows users to explore five curated examples. Data on this map shows results from Example 1: November 2019 rainfall-triggered mass wasting, West Pokot County, Kenya. C) Users can display  $rdNDVI$  results from a single point by clicking at a location on the map. The displayed result is in the format “(latitude, longitude),  $rdNDVI$  result.” D) The parameters window allows users to select the various input values, as further explained in Table 1. This panel also contains the Download button, which initiates the population of download links as seen in E. E) Download links for the resulting datasets allows users to save data directly to their local disk for further analysis and processing as desired. If any digitized geometries are present, a Digitized Geometries link will allow users to save a Google Earth compatible KML file. F) A Layers pane contains four consistent layers, including a hillshade DEM, the greenest composite pre- and post-event composite pixel images, and the  $rdNDVI$  image. Users can choose to turn on/off each layer as well as adjust the layer transparency. G) The default basemaps available in Google Earth Engine include satellite imagery with or without labels and a standard borders map with or without terrain data. Notice that the URL reflects current HazMapper parameters. URLs are automatically updated during use of the app. This design feature facilitates sharing of finds in HazMapper amongst colleagues by simply copying and pasting the URL into an email, or instant message chat screen, for example.

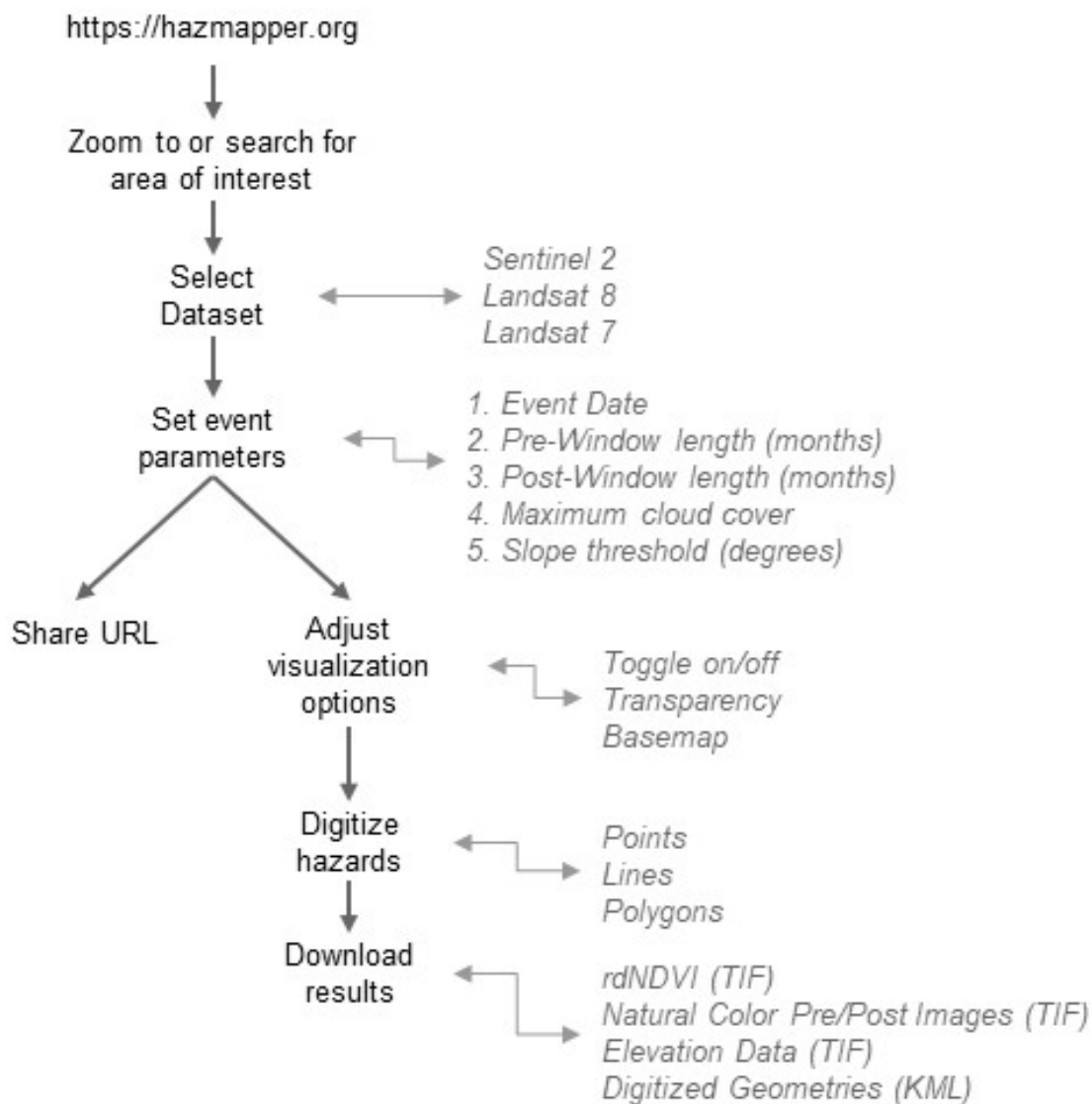


**Figure 2.** Suggested HazMapper workflows, including a branching point to share the URL or continue with analysis. Workflow culminates in downloading tagged image files (TIF) suitable for input into a GIS for advanced analysis or visualization functions. If the user digitizes key areas of interest, or hazards such as mass wasting processes, burn, or inundation extents, these can be exported as keyhole markup language (KML) files for sharing or viewing in Google Earth.

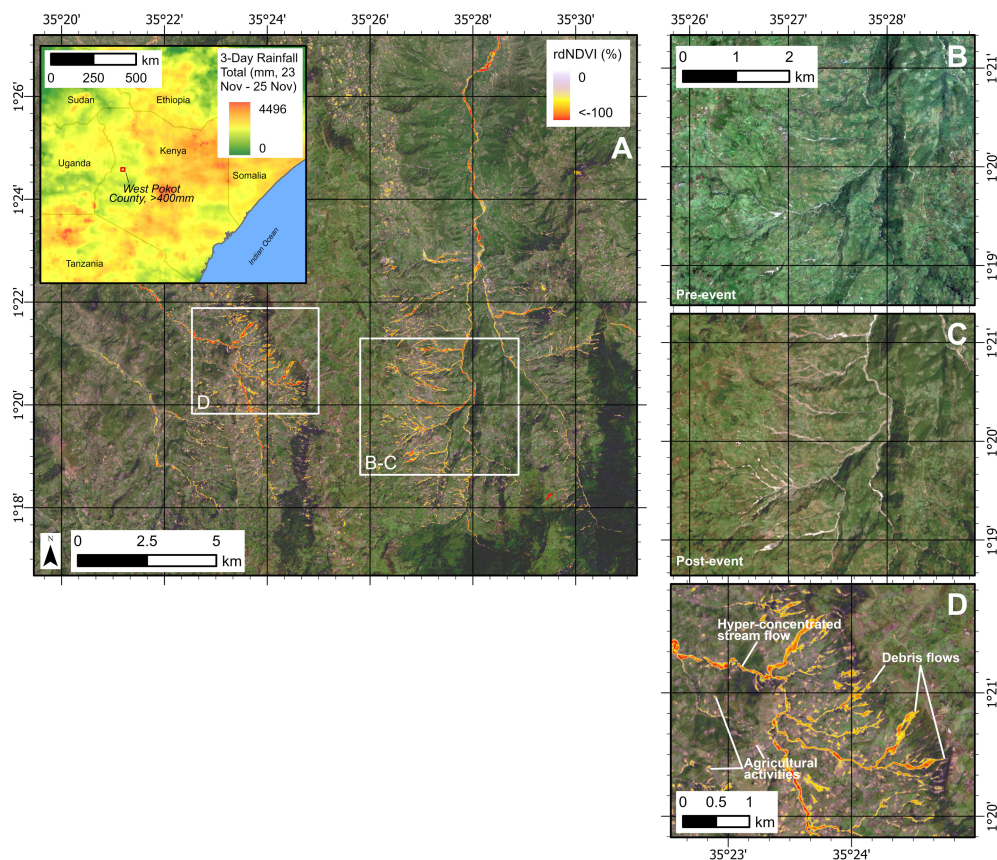


**Figure 3.** *rdNDVI* change detection images and greenest pixel composites following the 23 November 2019 rainfall-induced mass wasting event in West Pokot County, Kenya. See inset map for location and 3-day rainfall totals from storm, courtesy of NASA Integrated Multi-satellite Retrievals for GPM (IMERG) program. Parameters - Dataset: Sentinel-2, Event Date: 23 Nov 2019, Pre-Window: 2 months, Post-Window: 0.5 months, maximum cloud cover: 30%, and slope threshold: 0°. West Pokot County received >400 mm of rain in the 72-hour period 23-25 November, triggering landslides, debris flows, and floods during the heaviest rainfall on 23 November and subsequently hampering response efforts. A) *rdNDVI* illustrates hillslope and low-order stream channel disturbance, leading to debris-and-hyper concentrated flows and vegetation loss along river channels flowing toward the north and northwest. Landscape change is easier to interpret with *rdNDVI* compared to observations based only on pre- and post-event color images (B and C). Base image is post-event. B) Pre-event greenest pixel composite image showing relatively green vegetative cover across landscape. C) 0.5-month post-event greenest pixel composite illustrates reduction of vegetation in landslide and debris flow tracks and along river trunk channel. This reduction in vegetation is noted by negative *rdNDVI* values as seen in A. D) Close-up detail of negative *rdNDVI* values associated with mass wasting. Rectilinear patches of negative *rdNDVI* values in western area of panel D illustrate agricultural clearing or harvest activities across the event parameters. In mass wasting applications, further use of slope thresholding and interpretation based on landscape morphology will reduce these false positives. User interpretation of output *rdNDVI* polygon areas is always warranted in order to minimize false positives. B and C have the same map scale. A and D have the same *rdNDVI* color-scale. All maps have the same orientation. *rdNDVI* and greenest pixel composite data exported from HazMapper, available at <https://go.ncsu.edu/hazmapper-kenya>.

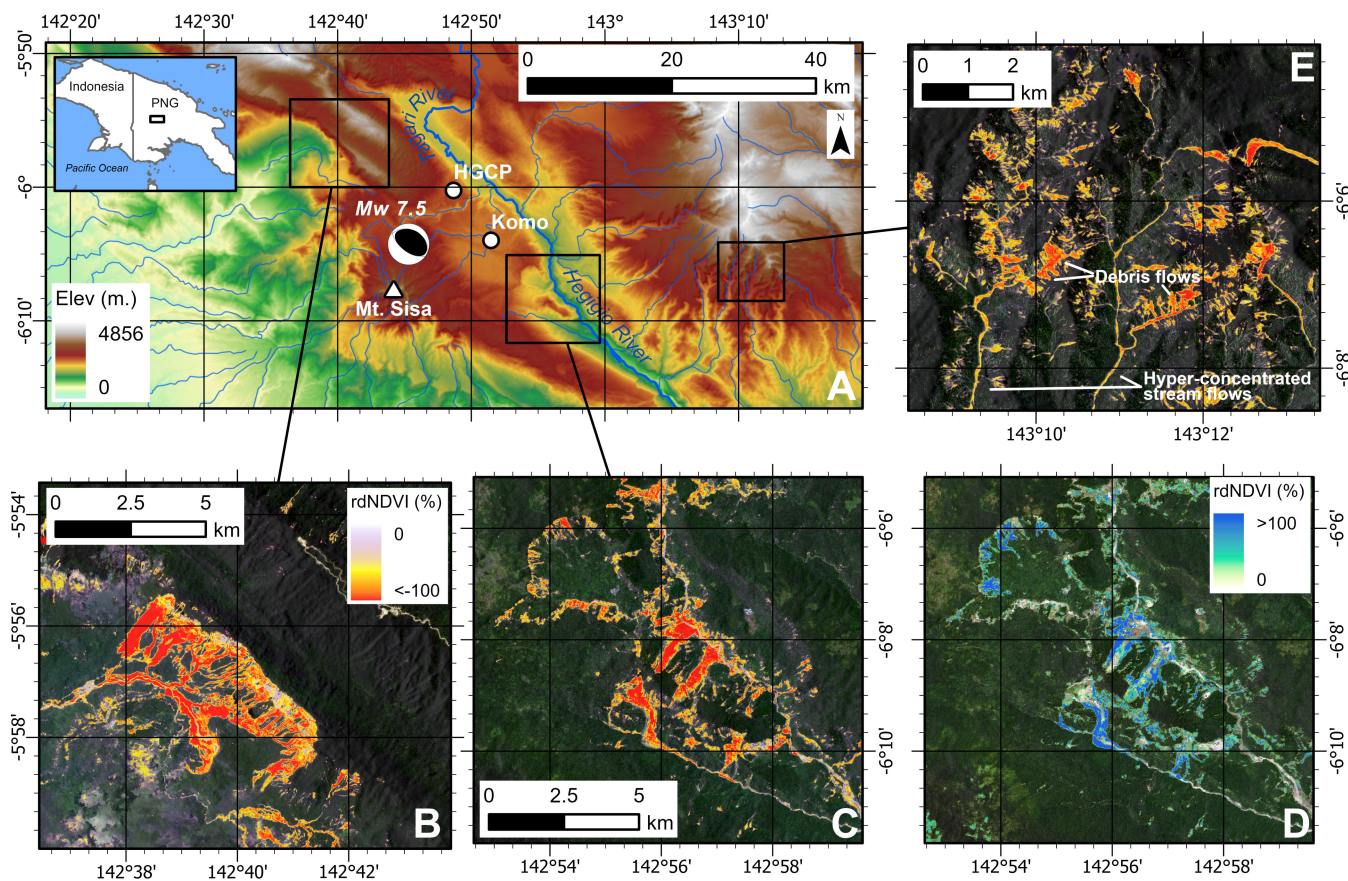


**Figure 4.** *rdNDVI* change detection images and greenest pixel composites following a landsliding event triggered by the  $M_w$  7.5, 26 February, 2018 earthquake in the Southern Highlands of Papua New Guinea (PNG). Inset map shows location within the country. Parameters for A-D - Dataset: Sentinel-2, Event Date: 25 Feb 2018, Pre-Window: 12 months, Post-Window: 9 month, maximum cloud cover: 30%, and slope threshold:  $0.05^\circ$ . A) Elevation map for the Southern Highlands of PNG with epicenter (focal mechanism) plotted. HGCP = Hides Gas Conditioning Plant, an Exxon-Mobil liquefied natural gas plant. Komo is the nearest large town and Mt. Sisa is a stratovolcano to the south. B-D) Select areas with high mass wasting density and associated hyper-concentrated stream flows. Base images are the pre-event greenest pixel composite and B-D have the same *rdNDVI* color scale. E) Recovery change detection image illustrating increases in vegetation within areas of previous mass wasting. These increases in vegetation are expected to increase root mass and provide a stabilizing effect for exposed soils. Parameters - Dataset: Sentinel-2, Event Date: 26 Aug 2018, Pre-Window: 6 months, Post-Window: 6 month, maximum cloud cover: 30%, and slope threshold:  $0.05^\circ$ . All maps have the same orientation. *rdNDVI* and greenest pixel composite data exported from HazMapper, available at <https://go.ncsu.edu/hazmapper-png>.

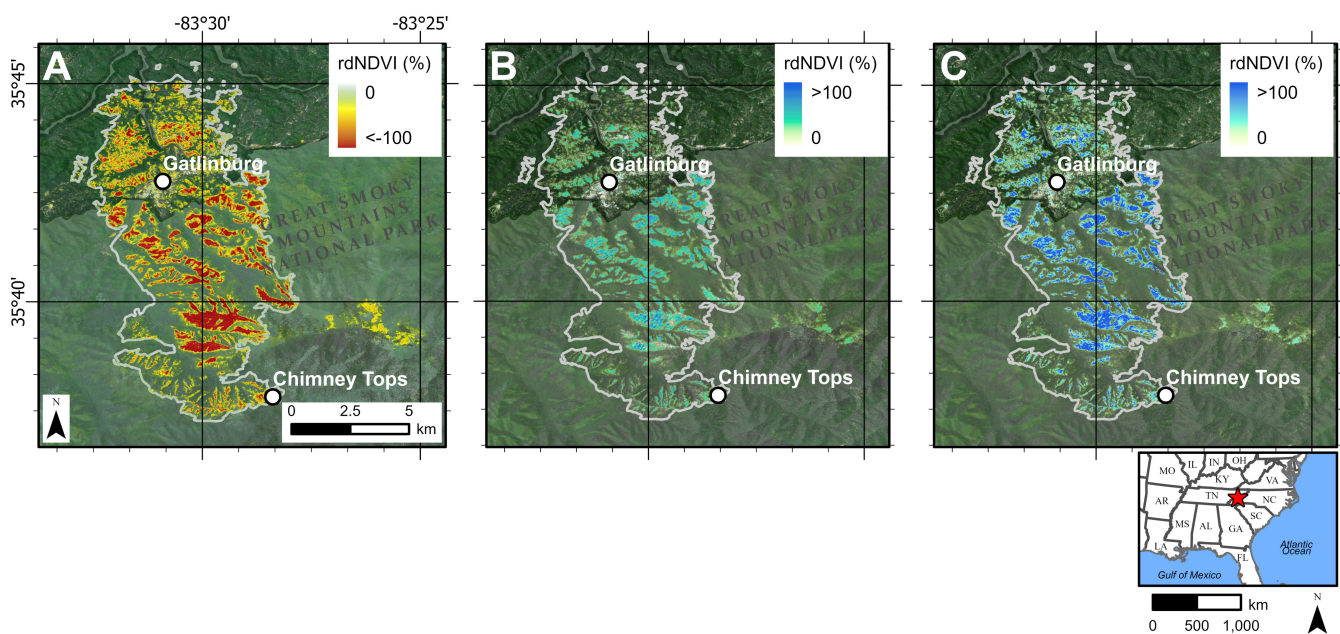


**Figure 5.** *rdNDVI* change detection images of vegetation loss and recovery during and following the Chimney Tops 2 fire that impacted Gatlinburg, Tennessee, USA and surrounding communities in November - December, 2016 (see location map to right). A) *rdNDVI* illustrates vegetative loss during the fire. Gray line is the published extent of the burn (USGS, 2020). Note the preferential vegetative loss (burn) along ridgetops. Base image is pre-event. Parameters - Event Date: 13 Dec 2016, Pre-Window: 12 months, Post-Window: 9 months. B) Change detection image of *rdNDVI* illustrating vegetative recovery between the first (2017) and second (2018) growing seasons following the fire. Base image is post-event. Parameters - Event Date: 13 Dec 2017, Pre-Window: 12 months, Post-Window: 12 months. C) Vegetative recovery (*rdNDVI*) between the first (2017) and third (2019) growing seasons following the fire. Note the general pattern of continuation and expansion of re-greening of the landscape, indicated by generally higher *rdNDVI* values (blues). Base image is post-event. Parameters - Event Date: 13 Dec 2017, Pre-Window: 12 months, Post-Window: 24 months. For all panels, Dataset: Sentinel-2, maximum cloud cover: 30%, and slope threshold: 0°. All maps have the same scale and orientation. *rdNDVI* and greenest pixel composite data exported from HazMapper, available from <https://go.ncsu.edu/hazmapper-chimneytops>.

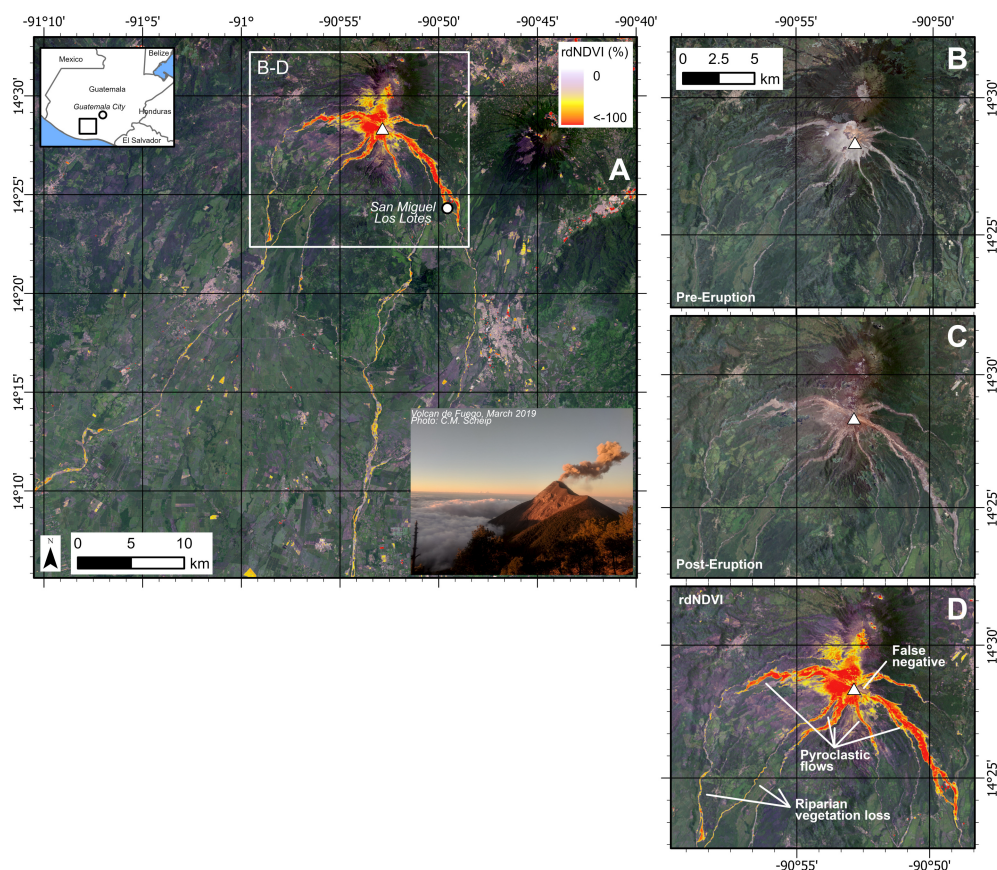


**Figure 6.** *rdNDVI* change detection images and greenest pixel composites following the 3-5 June 2018 volcanic eruption of Volcan de Fuego 40 km southwest of Guatemala City, Guatemala. White triangle denotes summit. Parameters - Dataset: Landsat-8, Event Date: 3 June 2018, Pre-Window: 12 months, Post-Window: 3 months, maximum cloud cover: 30%, and slope threshold:  $0.05^\circ$ . A) *rdNDVI* across the event illustrates loss of vegetation on upper flanks of the volcano summit and influence of pyroclastic flows on volcano flanks and downstream areas. San Miguel Los Lotes is a small community on the southeastern flanks of Volcan de Fuego that was heavily impacted during the eruption, including at least 25 fatalities. Note significant riparian vegetation loss in channels flowing south to southwest away from volcano. Base image is post-eruption. B-D) Close-up detail of Volcan de Fuego. B) Pre-eruption greenest pixel composite image of volcano. Note limited vegetation near summit. C) Detail image of volcano summit post-eruption greenest pixel composite. A typical color composite pre-post comparison can be performed to locate areas impacted by the eruption and resulting pyroclastic flows, however, *rdNDVI* as shown in D provides a more rapid approach to identifying impacted areas and adds additional detail such as riparian vegetation loss that is more difficult to observe in a standard (R,G,B) color image comparison. D) *rdNDVI* of the volcano following the eruption with notable observations annotated. B-D have the same scale. A and D use the same *rdNDVI* color-scale. All maps have the same orientation. *rdNDVI* and greenest pixel composite data exported from HazMapper, available at <https://go.ncsu.edu/hazmapper-fuego>.

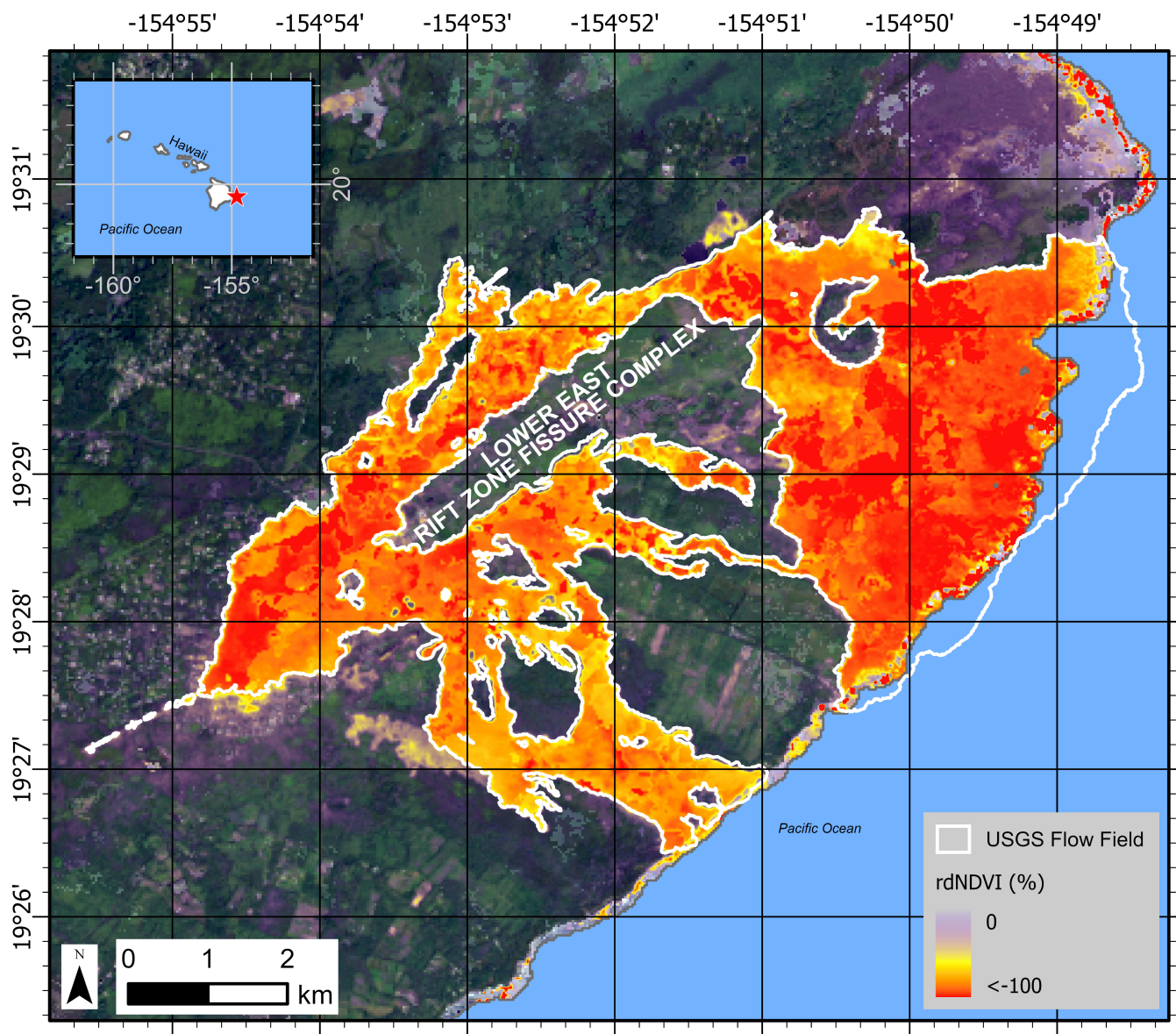


**Figure 7.** *rdNDVI* change detection images and greenest pixel composites following 3 May - 4 September 2018 Lower East Rift Zone eruption of Kīlauea volcano, Hawaii, USA. Parameters - Dataset: Landsat-8, Event Date: 4 September 2018, Pre-Window: 12 months, Post-Window: 6 months, maximum cloud cover: 30%, and slope threshold: 0.05°. *rdNDVI* across the event illustrates loss of vegetation. Base image is post-eruption. White line is the published lava flow field extent (Hawaiian Volcano Observatory staff, 2018) for comparison to the HazMapper result. Notice the additional land mass added to the island by the eruption that is encapsulated by the lava flow perimeter polygon. Because there was no vegetation in this area before and after the eruption, the *rdNDVI* method does not account for the new landmass. In future analyses, however, we expect to be able to identify vegetation growth on the landmass. *rdNDVI* and greenest pixel composite data exported from HazMapper, available at <https://go.ncsu.edu/hazmapper-lerz>.